Towards artificial photosynthesis on the lipid bilayer of liposomes

Klein, D.M.

Chapter 3

Influence of the alkyl chain length of liposome-supported photosensitisers and catalysts for photocatalytic CO_2 reduction

*Covalent functionalisation with alkyl tails is a common method for supporting molecular catalysts and photosensitisers onto lipid bilayers, but the influence of the alkyl chain length on the photocatalytic performances of the resulting liposomes is not well understood. In this work, we first prepared a series of rhenium-based CO_2-reduction catalysts [Re(4,4'-(C_nH_{2n+1})$_2$-bpy)(CO)$_3$Cl] (**ReC$_n$**; 4,4'-(C_nH_{2n+1})$_2$-bpy = 4,4'-dialkyl-2,2'-bipyridine) and ruthenium-based photosensitisers [Ru(bpy)$_2$(4,4'-(C_nH_{2n+1})$_2$-bpy)](PF$_6$)$_2$ (**RuC$_n$**) with different alkyl chain lengths (n = 0, 9, 12, 15, 17, and 19). We then prepared a series of PEGylated DPPC liposomes containing **RuC$_n$** and **ReC$_n$**, hereafter noted **C$_n$**, to perform photocatalytic CO_2 reduction in the presence of sodium ascorbate. The photocatalytic performance of the **C$_n$** liposomes was found to depend on the alkyl tail length, as the turnover number for CO (TON) was inversely correlated to the alkyl chain length, with a more than fivefold higher CO production (TON = 14.5) for the **C$_9$** liposomes, compared to **C$_{19}$** (TON = 2.8). Based on immobilisation efficiency quantification, diffusion kinetics, and time-resolved spectroscopy, we identified the main reason for this trend: two types of membrane-bound **RuC$_n$** species can be found in the membrane, either deeply buried in the bilayer and diffusing slowly, or less buried with much faster diffusion kinetics. Our data suggest that the higher photocatalytic performance of the **C$_9$** system is due to the higher fraction of the more mobile and less buried molecular species, which leads to enhanced electron transfer kinetics between **RuC$_9$** and **ReC$_9$**.*

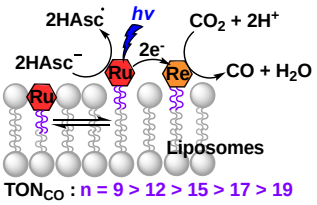

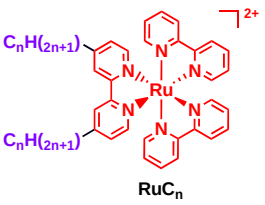

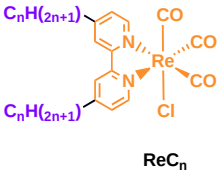

This chapter has been published as a full paper: David M. Klein, Santiago Rodríguez-Jiménez, Marlene E. Hoefnagel, Andrea Pannwitz, Amrutha Prabhakaran, Maxime A. Siegler, Tia E. Keyes, Erwin Reisner, Albert M. Brouwer, and Sylvestre Bonnet, *Chemistry – A European Journal* **2021**, 27, 17203-17212.

3.1 Introduction

Artificial photosynthesis has recognised potential to produce fuels in a sustainable way from earth-abundant resources such as water, carbon dioxide (CO_2), and sunlight.[1] In an artificial photosynthetic system, two half-reactions, such as water oxidation and CO_2 reduction, have to be combined, which requires control of light harvesting by photosensitisers, electron relays, and electron transfer to and from catalysts.[1] In natural photosynthesis, the efficiency and directionality of electron transfer is maximised by compartmentalisation, which consists in embedding the key components of the system, i.e., the oxygen evolving complex, photosystem I and II, and natural electron relays, within the lipid bilayer of the thylakoid membrane. A promising approach for artificial photosynthesis is to use lipid-based supramolecular assemblies, such as liposomes, as artificial mimics of thylakoid membranes. Photocatalytic liposomes represent a versatile platform for the co-embedding of catalysts and photosensitisers, as they are easy to prepare, allow one to solubilise apolar compounds in water, and can even facilitate charge separation.[1–3] In addition, they offer a unique way to compartmentalise molecular catalysts and photosensitisers in an aqueous environment, by keeping both types of molecules close to the water-bilayer interface and close to each other, thereby enhancing electron transfer rates.[1–3]

A common way to immobilise photochemically or catalytically active metal complexes onto the lipid bilayer of liposomes is by increasing their lipophilicity via functionalisation with alkyl tails. When a metal-containing complex is hydrophilic enough, the resulting alkyl-functionalised molecule *a priori* resembles an amphiphile, which allows it to self-assemble within the liposome bilayer. On the other hand, the metal head group of such amphiphiles bears the catalytically active centre; it should hence be close enough to the bulk water phase in order to be able to accept electrons and protons from the bulk aqueous environment. Such an immobilisation strategy has been employed by different groups in the context of solar fuels; for example, photocatalytic water oxidation with liposomes was

demonstrated using alkylated Ru-based water oxidation catalysts and photosensitisers bearing C_{12} tails[4,5]; hydrogen evolution was achieved using a C_{12}-alkylated cobaloxime-based hydrogen evolution catalyst and a C_{12}-alkylated Ru photosensitiser[6]; and a C_{13}-alkylated rhenium-based CO_2 reduction catalyst was used in combination with a C_{13}-alkylated Ru-based photosensitiser[7]. These studies focussed primarily on optimising the photocatalytic reaction by choosing the most efficient photosensitiser and catalyst; varying the fluidity of the lipid bilayer using unsaturated or saturated lipids; changing the light intensity and the concentrations of the catalysts, photosensitisers, and electron mediators; and overall comparing the photocatalytic mechanism on liposomes with that observed in homogeneous conditions. All studies concur that the photocatalytic mechanism on liposomes is strongly influenced by the confinement of the photosensitiser and catalyst to the same two-dimensional medium. However, so far, the alkyl chain length of such amphiphilic photosensitisers and catalysts seems to have been chosen according to synthetic availability or simply by chance, while the influence of the alkyl chain length on the photocatalytic performance of these systems has not been studied. Changing the alkyl chain length of an amphiphilic metal complex might modify the efficacy of membrane functionalisation or the location of the molecule within the lipid membrane. For example, a study by Ohba *et al.*[8] showed that the yields for chemically-driven water oxidation on liposomes could be enhanced by varying the length of the linker between ruthenium and the cholesterol group of a membrane-embedded water oxidation catalyst. Overall, the concentration and position of the photochemically and catalytically active molecules in the membrane are known to influence their photocatalytic or electron transfer properties; they should hence play a critical role in photocatalysis. Last but not least, as time-resolved spectroscopy studies in photocatalytic liposome are scarce, our understanding of their supramolecular photochemistry remains limited.

To address these knowledge gaps, we prepared here a series of rhenium-based CO_2-reduction catalysts [Re(bpy-(4,4'-C_n)$_2$)(CO)$_3$Cl] (**ReC$_n$**; (bpy-(4,4'-C_n)$_2$ = 4,4'-di-X-2,2'-bipyridine; X = C_nH_{2n+1} with n = 0, 9, 12, 15, 17, and 19) and a series of ruthenium-based photosensitisers [Ru(bpy)$_2$(bpy-(4,4'-

$C_n)_2)](PF_6)_2$ (**RuC$_n$**; n = 0, 9, 12, 15, 17, and 19) and used them for photocatalytic CO_2 reduction on PEGylated DPPC liposomes (hereafter noted **C$_n$**). The choice of this type of ruthenium photosensitisers was based on their known ability, both in terms of redox potential in the ground state and energy in the excited state, to fuel CO_2 reduction catalysed with rhenium catalysts.[7,9–12] The choice of the rhenium catalyst was based on the synthetic rationale that once prepared for the series of Ru-based photosensitiser, the series of bisalkylated 2,2'-bipyridine ligands with different chain lengths could be coordinated also to rhenium to make, in one step, a series of CO_2 reduction catalyst molecules with different chain lengths. In addition, the [Re(bpy)(CO)$_3$Cl] catalyst discovered by Lehn and co-workers[12] is one of the most studied CO_2-reduction catalysts, for which much information is available in the literature, for example about its CO_2 reduction mechanism. It must be noted, however, that the supramolecular properties of both types of molecules and their assembly in lipid membranes were expected to be different because of the neutral charge of the rhenium catalysts, compared to the dicationic nature of the ruthenium photosensitisers. In this work, we studied the photocatalytic performance of liposomes containing both molecules for CO_2 reduction using ascorbate ($HAsc^-$) as electron donor (Figure 3.1).

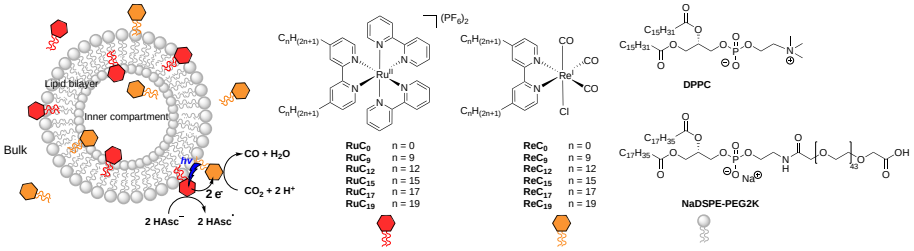

Figure 3.1. Formulae and naming of the ruthenium photosensitisers (red), rhenium catalysts (orange), and lipids (grey) used for photocatalytic CO_2 reduction on liposomes.

To understand the obtained photocatalytic results, we quantified the number of complexes that were actually immobilised on the liposome using inductively-coupled plasma mass-spectrometry (ICP-MS), and performed time-resolved spectroscopic and two-dimensional diffusion studies to assess the influence of the chain length on the electron transfer and molecular

diffusion in the membrane. We unravelled the existence of two types of photosensitiser species, one deeply embedded in the membrane that diffuses slowly and represents a dead-end for electron transfer and hence photocatalysis; and another one diffusing faster in the membrane leading to improved electron transfer. This fast-diffusing species must be located closer to the aqueous phase and plays therefore a major role in photocatalysis.

3.2 Results and Discussion

Synthesis and preparation of liposomes. A series of bis-alkylated ruthenium tris-bipyridine **RuC$_n$** and bis-alkylated rhenium tris(carbonyl) complexes **ReC$_n$** (Figure 3.1) were synthesised and characterised as described in the experimental part (see Appendix C). Then a series of liposome samples were prepared containing either one or both metal complexes with the same alkyl chain length; for example, the photocatalytic **C$_9$** liposome system contained **RuC$_9$** and **ReC$_9$**. For liposome preparation, the metal complexes were mixed with the respective lipid (either DMPC (1,2-dimyristoyl-*sn*-glycero-3-phosphocholine), DPPC (1,2-dipalmitoyl-*sn*-glycero-3-phosphocholine), or DSPC (1,2-distearoyl-*sn*-glycero-3-phosphocholine)) in organic solvents. 1,2-distearoyl-*sn*-glycero-3-phosphoethanolamine. N-(carbonyl-methoxypolyethylene glycol-2000) (NaDSPE-PEG2K) was added to the liposome formulation, which is known to stabilise liposome suspensions by avoiding aggregation.[4] Thorough evaporation of the organic solvent and hydration with a phosphate buffered solution (0.1 M, pH = 7.7), several freeze-thawing cycles, and standard extrusion through a 0.2 µm polycarbonate filter, afforded the liposomes (lipid:NaDSPE-PEG2K:**RuC$_n$**:**ReC$_n$** in a typical ratio of 100:1.0:X:Y with X = 0.0 or 0.4 and Y = 0.0 or 0.4). The liposome samples containing one or both metal complexes were characterised by dynamic light scattering to obtain the average diameter (Z_{ave}) and the polydispersity index (PDI) of the liposomes and by spectroscopic techniques to obtain the absorption maximum (λ_{abs}) and emission maximum (λ_{em}) of the metal complexes in the liposomes (see Tables C1, C2, C3, and C4 in Appendix C). Z_{ave} was typically found to be 120 – 140 nm for DMPC liposomes, 140 – 150 nm for DPPC liposomes, and 150 – 170 nm

for DSPC liposomes, with PDI values below 0.20 that indicated a uniform size distribution. The absorption and emission maxima for the ruthenium complexes (**RuC$_9$** – **RuC$_{19}$**, λ_{abs} = 424 – 465 nm and λ_{em} = 625 – 634 nm) and the emission maxima for the rhenium complexes (**ReC$_9$** – **ReC$_{19}$**, λ_{em} = 510 – 554 nm) immobilised on liposomes (Table C1 and Figure C1 for two representative examples) were comparable to literature values for **RuC$_{13}$** and **ReC$_{13}$** immobilised on DPPC vesicles.[7] λ_{abs} could not be determined for the rhenium complexes by UV-Vis spectroscopy due to lipid scattering in the region where rhenium absorbs (λ_{abs} = 380 nm in chloroform). Liposomes containing both metal complexes showed similar emission maxima for the ruthenium complexes (λ_{em} = 607 – 632 nm) and for the rhenium complexes (λ_{em} = 555 – 556 nm) immobilised on liposomes (Table C2), thus demonstrating that the spectroscopic features of the photosensitiser as well as of the catalyst are retained after incorporation into the liposome.

Influence of alkyl chain length on photocatalytic CO_2 reduction. Photocatalytic CO_2 reduction experiments were conducted with DPPC:NaDSPE-PEG2K:**RuC$_n$**:**ReC$_n$** (100:1.0:0.4:0.4) liposomes in CO_2-saturated aqueous phosphate solutions at pH 6.3 containing sodium ascorbate (NaHAsc, 0.1 M) as sacrificial electron donor (Figure 3.2 and Table C5). The gaseous products (CO and H_2) from photocatalytic reduction of aqueous CO_2 were quantified by gas chromatography, and the possible formation of formate in the aqueous phase was also monitored by IR and ^{1}H NMR spectroscopy. Three hours of UV- and blue light filtered simulated solar light irradiation were employed ($\lambda > 455$ nm, AM 1.5G, 100 mW cm^{-2}) to avoid photoexcitation of the Re(I) catalyst. CO evolved as the major product, with minor amounts of H_2 in all six photocatalytic **RuC$_n$-ReC$_n$** liposome systems, as reported in other rhenium-based CO_2-reduction catalytic systems that pointed already to the excellent selectivity of these catalysts.[7,11,13] The CO selectivity ranged between 97 – 99% for the **C$_9$-C$_{19}$** systems and 94% for the **C$_0$** system. Strikingly, a clear trend was observed: the photochemical performances of the photocatalytic liposomes were inversely correlated to the alkyl chain length, with the turnover number (TON = $n_{product}/n_{Re\text{-}catalyst}$) and photocatalytic turnover number (PTON = $2\times n_{product}/n_{Ru\text{-}photosensitiser}$; the factor

2 accounts for the fact that 2 molecules of photosensitiser must turnover once for the formation of one CO molecule) decreasing regularly from the **C_9** to the **C_{19}** system (Figure 3.2, Table C5, and C6, which give both η_{immob}-corrected and uncorrected TON and PTON, see below). The same trend was also observed for the turnover frequency (TOF = TON/time) and photocatalytic turnover frequency (PTOF = PTON/time). The **C_9** and **C_{12}** liposomes were hence the most active in reducing CO_2 to CO (81 – 109 nmol CO, TON = 10.8 – 14.5, PTON = 21.6 – 29.0, TOF = 4.3 – 5.7 h^{-1}, and PTOF = 8.7 – 11.3 h^{-1}), whereas the **C_{15}**, **C_{17}**, and **C_{19}** systems were much less active (21 – 41 nmol CO, TON = 2.8 – 5.5, PTON = 5.5 – 10.9, TOF = 1.1 – 2.0 h^{-1}, and PTOF = 2.3 – 3.9 h^{-1}). In all systems, a decrease in the TOF was observed after one hour, indicating that the systems were decomposing during irradiation, most probably due to the degradation of **RuC_n** as reported for the **C_{13}** system,[7] although the possible decomposition of **ReC_n** could not be discarded either on the basis of previous reports.[9,11]

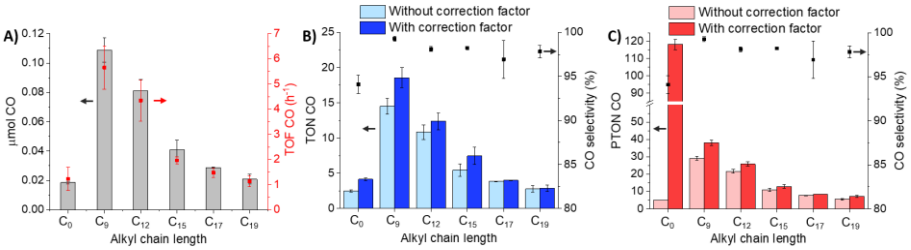

Figure 3.2. Photocatalytic activity after three hours of simulated solar light irradiation (λ > 455 nm, AM 1.5G, 100 mW cm^{-2}) as a function of alkyl chain length for DPPC liposomes containing **ReC_n-RuC_n** with same n: (A) evolved µmol of CO and uncorrected TOF CO; (B) (light blue) uncorrected and (dark blue) corrected TON CO and CO selectivity; (C) (light red) uncorrected and (dark red) corrected turnover number of CO produced per mol of photosensitiser (PTON CO) and CO selectivity. The TONs and TOFs were obtained after 3 h and 1 h, respectively. The applied correction factor (η_{immob}) can be found in Figure 3.4 and Table C9. Experimental conditions: [DPPC] = 625 µM, [DSPE-PEG2K] = 6.25 µM, [**ReC_n**] = 2.5 µM and [**RuC_n**] = 2.5 µM; CO_2-saturated 0.1 M NaH_2PO_4 and 0.1 M NaHAsc aqueous solution (3 mL, pH ≈ 6.3) at 25 °C. Bulk concentrations [**ReC_n**] and [**RuC_n**] indicate theoretical concentrations (before extrusion). Experiments were performed in triplicates.

For the most active system (**C_9**), the internal quantum yield for CO formation (Φ_{CO})[14] was calculated on the basis of the number of photons absorbed by

RuC$_9$ (see Equation C1 in Appendix C). In this calculation, Φ_{CO} was 0.048 ± 0.026% during the first hour of monochromatic visible light irradiation (λ = 455 nm). This value corresponded to a lower rate of CO production (0.04 μmol h^{-1}, TON = 11 after 2 h) compared to the **C$_{13}$** system published by Murata et al[7] (3.1 μmol h^{-1}, TON = 52 after 2 h). Such lower rate is probably a consequence of the lower concentration of the active components in our **C$_9$** system (0.4 mol% **RuC$_9$** and **ReC$_9$** in the membrane, 2.5 μM bulk concentration, 10^{-3} M local concentration for each complex), compared to the **C$_{13}$** system of Murata et al[7] (≈ 3.5 mol% **RuC$_{13}$** and **ReC$_{13}$** in the membrane, 40 μM bulk concentration, 10^{-2} M local concentration for each complex), which could lead to slower electron transfer between Ru and Re and/or more charge recombination, altogether decreasing the photocatalytic performance of the system. The **C$_0$** system in our study exhibited a particularly low activity (19 nmol CO, TON = 2.5, PTON = 5.0, TOF = 1.2 h^{-1}, and PTOF = 2.5 h^{-1}), but for such a system the **RuC$_0$** photosensitiser is hardly embedded in the membrane due to its low lipophilicity, while 62% of the **ReC$_0$** catalyst is embedded in the lipid bilayer, thus preventing efficient electron transfer (see section on immobilisation efficiency). Overall, our results not only highlight that alkyl chains are indeed required to immobilise both metal complexes onto photocatalytic liposomes, but they also strikingly demonstrate that a too long alkyl chain length is detrimental towards the photocatalytic performance of the system, and that shorter alkyl tails (**C$_9$** and **C$_{12}$**) give much better photocatalytic results.

Control experiments were performed to verify a few basic assumptions in this system. First, dynamic light scattering measurements were carried out to monitor the changes in size of the liposomes before and after photocatalysis. The average size of 150 ± 16 nm obtained before irradiation, and 161 ± 15 nm obtained after three hours irradiation (Table C3, Appendix C), were very similar, indicating that the liposomes remained essentially intact during photocatalysis. Second, UV-filtered but blue light-containing beam (λ > 400 nm) led to analogous photocatalytic performances compared to the above conditions where UV and blue filters were used (Figures C2 and C3). These results suggest that the main path for photocatalytic CO_2

reduction, even when the light beam contains blue light capable of exciting the rhenium complex, is photoexcitation of the **RuC$_n$** photosensitiser, followed by reductive quenching by ascorbate, and further electron transfer from the reduced **RuC$_n^-$** photosensitiser species to the **ReC$_n$** catalyst, as proposed by Murata and co-workers.[7] Third, experiments performed with the **C$_9$** system in absence of one of the components (Table C7) confirmed that neither CO nor H_2 evolved when **RuC$_9$**, NaHAsc, or visible light irradiation were absent. In the absence of **ReC$_9$**, only 0.2 ± 0.1 nmol of CO was detected, compared to 108.9 ± 8.3 nmol of CO when all components were present. This small amount of CO was probably produced by **RuC$_9$** or unidentified photodegradated by-products, as suggested previously.[10,15–19] Fourth, isotopic labelling experiments using $^{13}CO_2$ confirmed that ^{13}CO evolved as the only photocatalytic CO_2 reduction product, and no other CO_2 reduction products such as formate were detected after three-hour experiments using IR and ^1H NMR spectroscopy (Figures C4 and C5). Overall, all controls point to the well-behaved performance of this system: the catalysis really takes place at the surface of the liposome with membrane-embedded species, which remain stable during irradiation.

Understanding the tail-dependent photocatalytic behaviour. The more than five-fold difference in TON between **C$_9$** and **C$_{19}$** systems is worth mentioning, as elongating the alkyl chains may be conceptualised as a way to enhance membrane embedding of the functional molecules, thereby enhancing photocatalytic properties. Importantly, the lower photocatalytic activity observed with longer alkyl chains could not be explained by a change in the redox potentials of the complexes from **C$_9$** up to **C$_{19}$**. These redox potentials indeed hardly differed when alkyl chain lengths varied (i.e. $Ru^{2+/+}$ = –1.76 V for **RuC$_9$** and –1.70 V for **RuC$_{15}$**, Re^+/Re = –1.83 V for **ReC$_9$** and –1.83 V for **ReC$_{15}$**, measured in acetonitrile, and referenced versus Fc^+/Fc, Figures C6, C7, C8, and Table C8), even if the irreversibility of the **RuC$_{17}$** and **RuC$_{19}$** complexes in such conditions prevented reliable measurement of redox potentials. Thus, we turned to other methods, i.e., immobilisation efficiency quantification, transient absorption spectroscopy, and membrane diffusion measurements, to look for reasons behind the photocatalytic trend observed in Figure 3.2.

Immobilisation efficiency of ruthenium and rhenium complexes on liposomes. Liposome preparation contains many steps (Figure 3.3) including multiple hand-made filtrations through an extrusion filter, which may adsorb significant amounts of functional molecules depending on their solubility, their interaction with the filter material, or the pressure generated by the operator, as well as multiple cooling and heating steps, which are also potential sources of irreproducibility. Overall, the quantitative embedding of amphiphilic molecules in the membrane might be questioned. We hence engaged into measuring to what extent the alkyl tail length may influence the real efficiency of liposome immobilisation. Of course, preliminary confocal microscopy of **RuC$_{12}$**-containing multilamellar giant liposomes obtained before extrusion showed red emission (λ_{exc} = 488 nm and λ_{em} = 640 – 680 nm) coming only from the lipid bilayer (Figure C9), suggesting qualitatively that **RuC$_{12}$** was in majority taken up by the lipid bilayer itself. However, this technique was not quantitative, and it could not be used to study the photocatalytic liposomes obtained after extrusion and used for CO_2 reduction, as their hydrodynamic diameter (Z_{ave} < 200 nm) was significantly lower than the ultimate resolution of optical microscopy (~250-400 nm depending on wavelength).[20]

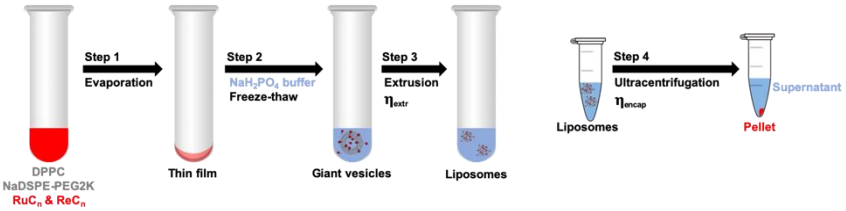

Figure 3.3. Stepwise preparation of photocatalytic liposomes and definition of the extrusion efficiency (η_{extr}) and encapsulation efficiency (η_{encap}, see main text).

Therefore, we used a more quantitative assay to address the immobilisation efficacy, which consisted in ultracentrifugating (at 100.4 kG) the metal-functionalised liposomes, and measuring the amount of metal complex in the supernatant after ultracentrifugation, either by UV-Vis spectroscopy or by ICP-MS. In this assay we considered a metal complex as “immobilised” in the liposome, if after ultracentrifugation it ended up in the centrifuged lipid pellet, and hence disappeared from the supernatant. As a note, we could not

distinguish whether the complex was entrapped in the inner aqueous compartment of the liposome, or really located inside the hydrophobic pocket of the lipid bilayer, as both cases led to entrapment in the lipid pellet. On the other hand, all molecules located in the outside bulk aqueous solution ended up in the supernatant and were hence considered as "non-immobilised".

This assay was realised in a first attempt by UV-Vis spectroscopy using liposomes containing a single type of metal complex (**RuC_n** or **ReC_n**). It showed that UV-Vis spectroscopy was not a suitable technique for quantification of the amount of liposome-immobilised metal complexes: before ultracentrifugation light scattering by the liposomes is significant in the blue and near-UV region of the spectrum where for example **RuC_{12}** (Figure C10) and **ReC_{12}** (Figure C11) absorb. The quantification of the initial amount of metal complex was hence not reproducible. As a consequence, we turned to ICP-MS analysis, with which it is possible to quantitatively and accurately determine the metal content (Ru and Re) of the liposome samples before extrusion, between extrusion and ultracentrifugation, or that of the supernatant after ultracentrifugation (see Figure 3.3). It is hence possible to measure experimentally the immobilisation efficiency (η_{immob}), defined as the amount of complex effectively present in the liposome, divided by the amount of complex introduced in the liposome formulation. Two phenomena during liposome preparation can lead to an immobilisation efficiency η_{immob} lower than unity (Equation 3.1): first, extrusion may lead to adsorption of some of the metal complex onto the extrusion filter (Figure C12), which lowers the quantity of metal complex effectively present in the extruded sample, compared to the amount theoretically introduced. We defined η_{extr} as the extrusion efficiency (step 3 in Figure 3.3) and quantified it by measuring the amount of Ru and Re effectively found in the liposome sample by ICP-MS after extrusion but before ultracentrifugation, and divided it by the theoretical amount of Ru and Re introduced in the liposome formulation (Equation 3.2). Second, depending on its total hydrophobicity, the amphiphilic complexes effectively present in the extruded sample may be distributed between the aqueous phase (interior or exterior) and the

hydrophobic environment of the membrane, rather than fully embedded in the membrane. In principle, higher alkyl chain lengths will increase lipophilicity and hence the amount of complex embedded in the lipid bilayer; but the extent of such embedding is usually not addressed and might have been over-evaluated in previous work, as it will depend on the hydrophilicity of the metal head as well. We hence defined the encapsulation efficiency, η_{encap}, as the molar fraction of metal complex entrapped in the lipid pellet obtained after ultracentrifugation, divided by the total amount of complex present in the extruded sample (before ultracentrifugation, step 4 in Figure 3.3).[21] η_{encap} is given by Equation 3.3. The final yield of complex immobilisation (η_{immob}) is the product of the extrusion yield η_{extr} with the encapsulation yield η_{encap} (Equation 3.1).

$$\eta_{\mathrm{immob}} = \eta_{\mathrm{extr}} \times \eta_{\mathrm{encap}} \qquad \text{Equation 3.1}$$

$$\eta_{\mathrm{extr}} = \frac{[\mathrm{metal}]_{\mathrm{liposomes}}}{[\mathrm{metal}]_{\mathrm{giant\ vesicles}}} \times 100\% \qquad \text{Equation 3.2}$$

$$\eta_{\mathrm{encap}} = \left(1 - \left(\frac{[\mathrm{metal}]_{\mathrm{supernatant}}}{[\mathrm{metal}]_{\mathrm{liposomes}}}\right)\right) \times 100\% \qquad \text{Equation 3.3}$$

The experimental values of η_{extr}, η_{encap}, and η_{immob} for photocatalytic liposome formulations containing both metal complexes (DPPC:NaDSPE-PEG2K:**RuC$_n$**:**ReC$_n$** in a ratio of 100:1.0:0.4:0.4) are shown in Figure 3.4 and Table C9. Interestingly, η_{extr} was high for **RuC$_0$** and **ReC$_0$** (> 95%) but moderately high (> 75%) for **RuC$_n$** and **ReC$_n$** with n > 9. Thus, a considerable amount of compound was lost during extrusion, as visually observed by a yellowish-orange deposit on the polycarbonate filter (Figure C12). These losses were essentially independent of the alkyl chain length. We attribute the significant error bars in η_{extr} (especially for **ReC$_9$**, **ReC$_{12}$**, and **ReC$_{15}$**) to the complexity of the extrusion procedure (e.g., tricky temperature control, minute variations of the manual pressure during extrusion, or different amounts of time between the different steps of multiple extrusion) and to the dynamics of such a supramolecular system. The low η_{encap} value for **RuC$_0$** (< 5%) and the moderate η_{encap} for **ReC$_0$** (62%) demonstrate the crucial role of alkyl tails for the immobilisation of such complexes in lipid bilayers. In both

cases the supernatant was very colourful and the liposome pellet was colourless (Figure C13, left) in contrast to for example **C_9** liposomes for which the supernatant was poorly coloured compared to the lipid pellet (Figure C13, right). In contrast, for **RuC_n** and **ReC_n**, η_{encap} was close to 100% in all n ≥ 9 cases. Thus, with these particular metal-containing heads the alkyl chain length did not affect η_{encap} significantly, as long as alkyl tails were present (n ≥ 9), and all molecules that did not stay in the extrusion filter effectively ended up immobilised within the membrane. Most importantly, the variation of η_{immob} with n did not provide an explanation for the trend observed in Figure 3.2: the most hydrophobic **RuC_n** and **ReC_n** complexes were rather efficiently immobilised in the liposomes, hence the lower photocatalytic efficacy of the **C_{17}** and **C_{19}** liposomes could not be explained by a lower immobilisation efficacy of its molecular components in the membrane. It should be noted, however, that the losses during immobilisation, which are essentially due to the losses during extrusion, are crucial to correctly calculate turnover numbers and turnover frequencies in photocatalytic experiments with liposomes (e.g. TON and PTON). Without such corrections the PS or catalyst concentration will be over evaluated and hence the (P)TONs and (P)TOFs systematically underestimated.

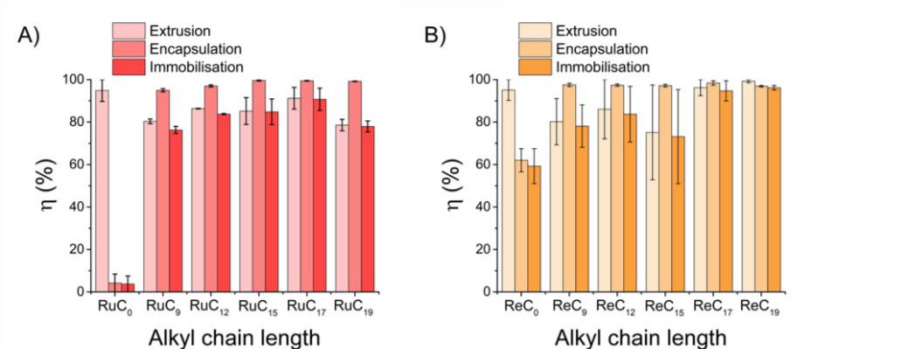

Figure 3.4. Evolution of the extrusion (η_{extr}), encapsulation (η_{encap}), and immobilisation (η_{immob}) efficiencies versus alkyl chain length for DPPC liposomes containing **RuC_n** and **ReC_n** with the same n. A) and B) show the data for ruthenium and rhenium, respectively. Experimental conditions before extrusion: [DPPC] = 6.25 mM, [NaDSPE-PEG2K] = 62.5 μM, [**ReC_n**] = 25 μM and [**RuC_n**] = 25 μM in 0.1 M NaH_2PO_4 buffer. Efficiencies are indicated as an average from two independent liposome preparations; error bars correspond to the average deviation from the mean.

Transient absorption spectroscopy study. As the lower photocatalytic activity of the liposomes containing the more hydrophobic amphiphiles could not be explained by problems during liposome preparation, we analysed two liposome systems in more detail using transient absorption (TA) spectroscopy, focusing on the ones containing the shortest (**C_9**) and longest (**C_{19}**) tails in the series. In these TA experiments, we followed the quenching of the key photoreduced intermediate in the membrane, **RuC_n^-** (similar to $[Ru(bpy)_3]^+$, reported at $\lambda_{max} \approx 505$ nm, $\varepsilon_{505nm} = 1.2 \times 10^4$ $M^{-1}cm^{-1}$ in acetonitrile[22]), by the catalyst **ReC_n** present at either 0.0, 0.4, or 1.6 mol% in the membrane. **RuC_n^-** is obtained by the reductive quenching of the membrane-embedded excited state **RuC_n^*** (0.4 mol%) in presence of 0.1 M NaHAsc in the bulk aqueous phase. Under these conditions, **RuC_n^-** was formed within the first 40 ns (together with the ascorbate radical $HAsc^\bullet$) and its concentration kept increasing over at least 2 µs (Figure C14).[7] Its decay was monitored for up to 10 ms, as the clear signature peak of **RuC_n^-** near 505 nm was still visible after a very long time of 2 ms (Figure C15). The decay of **RuC_n^-** with and without **ReC_n** is shown in Figure 3.5 and Figure C16.

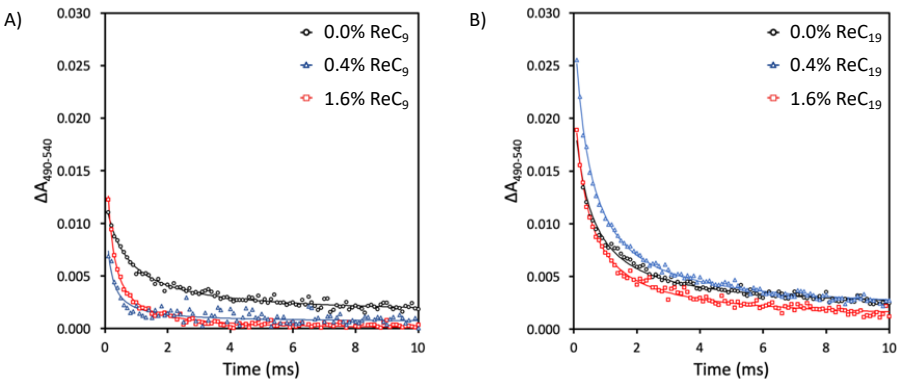

Figure 3.5. TA kinetic traces of photocatalytic DPPC liposomes containing 1 mol% NaDSPE-PEG2K, 0.4 mol% **RuC_n** and varying amounts of **ReC_n** (A: n = 9, B: n = 19), after laser excitation (λ_{exc} = 450 nm, 3.5 mJ per pulse) on a 10 ms timescale (timestep = 0.1 ms). The values for absorption were averaged between 490 – 540 nm. Experimental conditions: [DPPC] = 6.25 mM, [NaDSPE-PEG2K] = 62.5 µM, [**RuC_n**] = 25 µM, and [**ReC_n**] = 0, 25 or 100 µM in CO_2-saturated 0.1 M NaHAsc aqueous solution. Bulk concentrations [**ReC_n**] and [**RuC_n**] indicate theoretical concentrations (before extrusion).

The TA signature of $\mathbf{RuC_n^-}$ decayed in time following a non-exponential rate law. In the simplest model, in the absence of quencher $\mathbf{ReC_n}$, such a decay is a result of second-order charge recombination of $\mathbf{RuC_n^-}$ and $HAsc^\bullet$ with rate constant k_{CR}, both having identical initial concentration c_0 because they were formed together. The time-dependent concentration c(t) of the $\mathbf{RuC_n^-}$ intermediate is then given by Equation 3.4 (see Appendix C for mathematical derivation). The data obtained could not be fitted using this simple model, probably because of the disproportionation reaction of $HAsc^\bullet$, which lowered the effective amount of $HAsc^\bullet$ near the membrane and hence resulted in an excess of $\mathbf{RuC_n^-}$ remaining at long time scales (Figure 3.5A, black curve).[23] If the excess of unreacted $\mathbf{RuC_n^-}$ (c_∞) was included in the model (Equation 3.4), then the decay data could be fitted pretty well (Equation 3.5).

$$c(\mathrm{t}) = \frac{c_0}{1 + k_{\mathrm{CR}} c_0 t} \qquad \text{Equation 3.4}$$

$$c(\mathrm{t}) = \frac{c_0}{1 + k_{\mathrm{CR}} c_0 t} + c_\infty \qquad \text{Equation 3.5}$$

$$c(\mathrm{t}) = \frac{k_{\mathrm{Q}} c_0}{k_{\mathrm{Q}} e^{k_{\mathrm{Q}} t} + k_{\mathrm{CR}} c_0 (e^{k_{\mathrm{Q}} t} - 1)} \qquad \text{Equation 3.6}$$

In the presence of 0.4 mol% of the $\mathbf{ReC_n}$ quencher, the decay of the $\mathbf{RuC_n^-}$ absorption was faster, which can be described as a combination of first order quenching k_Q and second order charge recombination k_{CR} according to Equation 3.6.[24] The fit with Equation 3.6, however, showed a strong interdependence of the values of the fitted rate constants and the fit was not improved in comparison to Equation 3.5. In Figure 3.5, the blue and red decay curves show data fitting using Equation 3.5 (for fitting parameters see Table C10). Figure 3.5A shows a clear quenching of $\mathbf{RuC_9^-}$ by an increasing concentration of $\mathbf{ReC_9}$. The residual absorbance at longer times decreased significantly in comparison to the data obtained in absence of $\mathbf{ReC_9}$ in the membrane, which can be interpreted as the result of all $\mathbf{RuC_9^-}$ disappearing due to electron transfer to the $\mathbf{ReC_9}$. By contrast, the TA data obtained with $\mathbf{ReC_{19}}$ (Figure 3.5B) demonstrated that $\mathbf{RuC_{19}^-}$ was also quenched by the presence of the Re catalyst, but to a much smaller extent. Overall, these spectroscopic data strongly suggested that electron transfer from $\mathbf{RuC_n^-}$ to $\mathbf{ReC_n}$ was significantly faster in the case of the $\mathbf{C_9}$ system than with the $\mathbf{C_{19}}$

system. This observation would correlate with the lower photocatalytic performances of the liposome-embedded system with longer alkyl chains, if we assume that the redox and catalytic properties of the metal head of the amphiphilic complexes are independent from the chain length, which seems reasonable. To further investigate why the alkyl chain length strongly influenced the ability of these membrane-embedded molecules to transfer electrons, we went further into studying the mobility of the molecules in the membrane.

Lateral mobility of membrane-bound RuC_n. The rate of lateral diffusion of membrane-bound Ru and Re species will impact their collision frequency, which may impact intermolecular electron transfer kinetics. To investigate this hypothesis, we probed the diffusivity of the emissive **RuC_n** photosensitiser complexes in a model pore-supported lipid bilayer. In this experimental setup previously reported by some of us,[25,26] and coined "microcavity supported lipid bilayers" (MSLBs), the lipid bilayer is supported across aqueous-filled micron-diameter pore arrays, shown schematically in Figure C17. The lateral mobility of emissive molecules situated in the membranes located above the pores, because of the aqueous interface at both leaflets, was shown to be very similar to that observed in liposomes of the same composition.[27,28] The micron dimensions of the cavities and the good stability of the supported lipid membranes make this model highly amenable to study lateral diffusion by fluorescence correlation spectroscopy.[29] Due to experimental limitations it was not possible to obtain two-dimensional diffusion data for the **ReC_9** and **ReC_{19}** catalysts, so only the ruthenium photosensitisers were probed.

MSLBs comprised of DPPC:NaDSPE-PEG2K:**RuC_n** in a ratio $100:1:4\cdot10^{-4}$ were hence prepared on polydimethylsiloxane pore arrays supports by Langmuir-Blodgett deposition followed by fusion of vesicles reconstituted with the complexes. The emission lifetime images (Figure C17) show pore array with supported membrane labelled with DOPE-ATTO 655, which confirmed the formation of the bilayer. Autocorrelation functions (ACFs) from ruthenium emission were collected across 20 – 30 cavities per sample and averaged to obtain diffusion values. The diffusion coefficients of the **RuC_n** molecules were

calculated by fitting the ACF using the two-component model given in Appendix C (method section); the resulting data for the **RuC_9** and **RuC_{19}** complexes is given in Table 3.1. For comparison, the ACF was also collected for the free **RuC_{19}** complex in bulk acetonitrile and this data fit to a three-dimensional diffusion to obtain a typical bulk diffusion coefficient of 199 $\mu m^2 s^{-1}$ (Figure C17).

Table 3.1. ACF data of **RuC_n** in MSLBs consisting of DPPC:NaDSPE-PEG2K.

Complex	D_1 ($\mu m^2 s^{-1}$)	D_2 ($\mu m^2 s^{-1}$)	A_1 (%)	A_2 (%)	α_1	α_2
RuC_9	82 ± 7	0.3 ± 0.9	82	18	1.12 ± 0.07	0.64 ± 0.01
RuC_{19}	50 ± 2	0.4 ± 0.8	56	44	1.20 ± 0.05	0.98 ± 0.02

Figure 3.6 shows representative plots of fluorescence fluctuations (time-traces) and the corresponding ACFs obtained for **RuC_n** in MSLBs comprised of DPPC:NaDSPE-PEG2K:**RuC_n**. Interestingly, in both cases the ACFs showed two diffusing components from membrane-bound **RuC_n**: a slow one and a fast one. The two-dimensional diffusion coefficients of the slow-moving component for **RuC_9** and **RuC_{19}** were 0.3 ± 0.9 $\mu m^2 s^{-1}$ and 0.4 ± 0.8 $\mu m^2 s^{-1}$, respectively, which are identical within experimental error. These values are also consistent with the fluidity of a typical DPPC:NaDSPE-PEG2K bilayer at room temperature: the transition temperature of 41 °C for DPPC has been shown to be only modestly mitigated by the presence of 1 mol% NaDSPE-PEG2K,[30] so that the membrane is in the gel phase at room temperature, leading to typical two-dimensional diffusion coefficients below 1 $\mu m^2 s^{-1}$. By contrast, the diffusion values for the fast-moving component were 82 ± 7 $\mu m^2 s^{-1}$ and 49 ± 2 $\mu m^2 s^{-1}$ for **RuC_9** and **RuC_{19}**, respectively, which is on the one hand significantly faster than that of lipid probes fully embedded in the hydrophobic core of the membrane, but on the other hand much slower than the value measured for diffusion in bulk solution. The fast-moving components are hence tentatively attributed to **RuC_n** molecules that are clearly associated with the bilayer, but not deeply embedded into it. Alternatively, the fast-diffusing complexes may be associated with domains originating from NaDSPE-PEG2K.[31] As noted previously, fast super-diffusion can be observed at the membrane interface upon modification with PEG.[32] Super-diffusion is characterised by an anomalous factor (α) greater than 1

and such an α value was noted here. For the slow diffusion component, α is effectively 1 for **RuC$_{19}$**, indicating free Brownian diffusion, but α is below 1 for **RuC$_9$**, which may indicate some self-aggregation of the complex in the membrane, which would also be consistent with the time trace in Figure 3.6A that shows some clustered peaks.

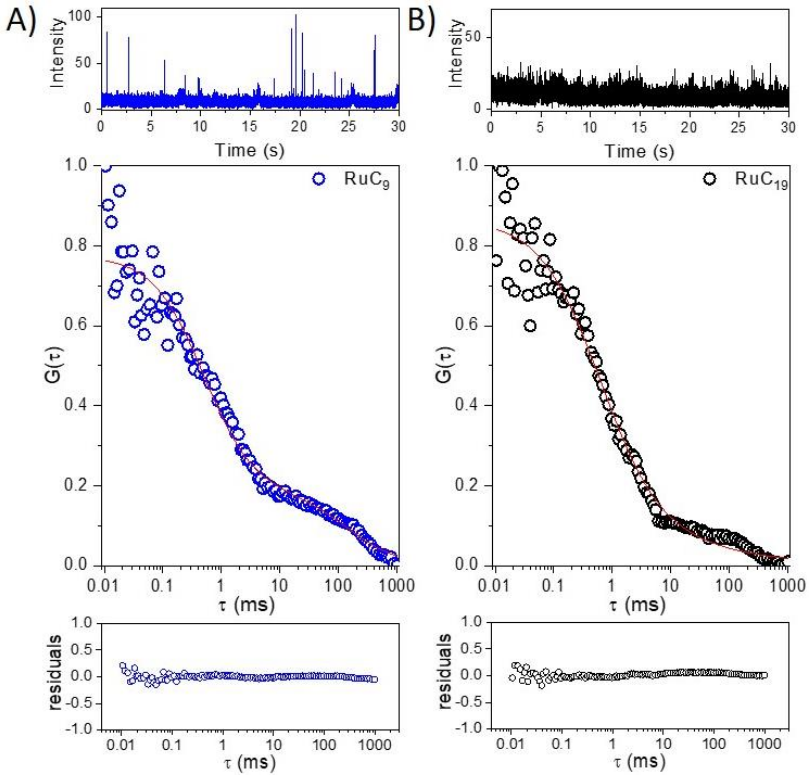

Figure 3.6. Representative intensity-time trace (top) and ACF (bottom) data measured over a single microcavity of MSLBs comprised of DPPC:NaDSPE-PEG2K:**RuC$_n$** in a ratio of 100:1:10^{-4} for (a) **RuC$_9$**, and (b) **RuC$_{19}$**. The fit ACF to the two-component model is shown as the red line and bottom shows the residuals, that indicate the quality of the fit to the two-dimensional model of diffusion. Experimental conditions: [DPPC] = 1.36 mM, [NaDSPE-PEG2K] = 13.6 μM, and [**RuC$_n$**] = 40 nM in phosphate buffer saline (pH = 7.7). Bulk concentration [**RuC$_n$**] indicates theoretical concentration (before extrusion).

Critically, the relative contribution or amplitude of the fast- and slow-diffusing components was found to vary with alkyl chain length. 82% of **RuC$_9$** constituted the fast component (D_1) in contrast to 56% for **RuC$_{19}$**. The

diffusion values for the fast component varied hence with the mass of the molecule, while the slow component did not. The latter observation was consistent with complexes that are well-embedded in the bilayer and essentially follow the diffusion rate of other lipids of the membranes; it hence directly reflects, as discussed above, the typical viscosity of a gel phase membrane at room temperature. However, the higher amplitude of the fast-diffusing component observed for **RuC_9**, correlates well with the higher photocatalytic performances of the **C_9** liposome system and faster electron transfer rate observed by TA spectroscopy, compared to the **C_{19}** system. The coexistence of two different types of membrane-embedded **RuC_n** species with two different diffusion coefficients, is, to our knowledge, unprecedented. It suggests that the fast-diffusing **RuC_n** molecules at the liposome interface participate primarily in the photocatalytic process, and that the higher proportion of fully-embedded and slowly-diffusing molecules obtained with more hydrophobic amphiphiles (here **RuC_{19}**, but also probably **ReC_{19}**) is responsible for the lowering of the electron transfer rates and the overall lower yields for photocatalytic CO_2 reduction in DPPC liposomes (Figure 3.7). It may even be that **RuC_{19}** species are just too slow-diffusing to have any significant collision frequency for efficient electron transfer, i.e., that they are photocatalytically "dead". In other words, when all redox and excited state properties of photosensitisers and catalysts are equal it is the lateral diffusion of the molecules within the lipid bilayer that determines the final efficacy of photocatalysis, so that shorter alkyl chains are actually better than longer ones. As a side note it is very difficult, on the basis of available experimental evidence, to be definitive about the orientation of particularly the fast-diffusing species with respect to the membrane. The diffusion coefficient of the slow-diffusing component is very similar to what would be expected for a gel phase lipid bilayer, which suggests that this fraction of the complex is incorporated into the membrane in a manner similar to the amphiphilic lipids, with the metal head group oriented close to the zwitterionic lipid head group at the aqueous interface, and the alkyl tail embedded into the hydrophobic core of the membrane. By contrast, the fast component may be lying along the membrane interface, i.e., be poorly embedded, or may be associated with PEG domains at the membrane interface. Also, the comparative roles of the relative orientation versus the

rate of diffusion of **ReC$_n$** and **RuC$_n$** are impossible to assess at this stage. More experiments and/or calculations would be needed draw a conclusion on this point.

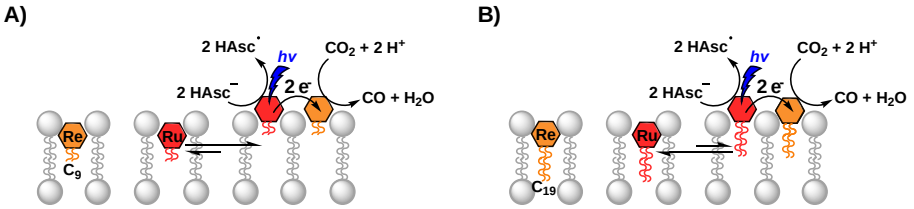

Figure 3.7. Proposed model for photocatalytic CO_2 reduction in DPPC lipid bilayers for a) the **C$_9$** system, where the amphiphilic **RuC$_9$** molecules in the membrane are less hydrophobic and hence primarily located near the water-membrane interface, where they diffuse faster and perform faster electron transfer to **ReC$_9$**; and b) the **C$_{19}$** system, where the amphiphilic **RuC$_{19}$** molecules are more hydrophobic and hence primarily deeply buried inside the hydrophobic core of the membrane, where they diffuse slower and perform slower electron transfer to **ReC$_{19}$**. Note: the real orientation of the alkyl tail is unknown and the drawing is not supposed to represent their real orientation in the membrane.

3.3 Conclusion

In this work, we observed that the photocatalytic performance of liposomes functionalised with amphiphilic ruthenium photosensitisers and CO_2-reducing rhenium catalysts is inversely correlated to the alkyl chain length of the amphiphilic molecules embedded in the membrane. In addition, we observed for the first time two co-existing types of amphiphilic ruthenium molecules **RuC$_n$** in these lipid bilayers: one slow-diffusing and deeply buried in the membrane, and another one diffusing much faster at the membrane-water interface, and prone to participate in electron transfer processes. Photocatalytic CO_2 reduction on liposomes hence requires careful optimisation of the alkyl chain length: no tail is detrimental to the immobilisation on the membrane, but chains that are too long lead to a larger fraction of deeply buried, slow-diffusing molecular species, leading to less efficient electron transfer and low photocatalytic performances. Overall, this works appears as an essential step towards increasing our fundamental understanding of the supramolecular- and photo-chemistry of amphiphilic

functional molecules inserted in lipid bilayers, which will be essential for the development of more efficient biomimetic systems for artificial photosynthesis.

3.4 References

1 A. Pannwitz, D. M. Klein, S. Rodríguez-Jiménez, C. Casadevall, H. Song, E. Reisner, L. Hammarström and S. Bonnet, *Chem. Soc. Rev.*, 2021, **50**, 4833–4855.

2 M. Hansen, S. Troppmann and B. König, *Chem. Eur. J.* , 2016, **22**, 58–72.

3 J. N. Robinson and D. J. Cole-Hamilton, *Chem. Soc. Rev.*, 1991, **20**, 49–94.

4 B. Limburg, J. Wermink, S. S. van Nielen, R. Kortlever, M. T. M. Koper, E. Bouwman and S. Bonnet, *ACS Catal.*, 2016, **6**, 5968–5977.

5 M. Hansen, F. Li, L. Sun and B. König, *Chem. Sci.*, 2014, **5**, 2683–2687.

6 S. Troppmann and B. König, *Chem. Eur. J.* , 2014, **20**, 14570–14574.

7 N. Ikuta, S. Y. Takizawa and S. Murata, *Photochem. Photobiol. Sci.*, 2014, **13**, 691–702.

8 T. Koshiyama, N. Kanda, K. Iwata, M. Honjo, S. Asada, T. Hatae, Y. Tsuji, M. Yoshida, M. Okamura, R. Kuga, S. Masaoka and M. Ohba, *Dalt. Trans.*, 2015, **44**, 15126–15129.

9 J. Hawecker, J.-M. Lehn and R. Ziessel, *Helv. Chim. Acta*, 1986, **69**, 1990–2012.

10 J. Hawecker, J.-M. Lehn and R. Ziessel, *J. Chem. Soc. Chem. Commun.*, 1985, 56–58.

11 G. Sahara and O. Ishitani, *Inorg. Chem.*, 2015, **54**, 5096–5104.

12 J. Hawecker, J.-M. Lehn and R. Ziessel, *J. Chem. Soc. Chem. Commun.*, 1984, 328–330.

13 A. Nakada, K. Koike, K. Maeda and O. Ishitani, *Green Chem.*, 2016, **18**, 139–143.

14 J. Bonin, M. Robert and M. Routier, *J. Am. Chem. Soc.*, 2014, **136**, 16768–16771.

15 A. Nakada, K. Koike, T. Nakashima, T. Morimoto and O. Ishitani, *Inorg. Chem.*, 2015, **54**, 1800–1807.

16 J. L. Grant, K. Goswami, L. O. Spreer, J. W. Otvos and M. Calvin, *J. Chem. Soc. Dalt. Trans.*, 1987, 2105–2109.

17 A. Call, M. Cibian, K. Yamamoto, T. Nakazono, K. Yamauchi and K. Sakai, *ACS Catal.*, 2019, **9**, 4867–4874.

18 P. L. Cheung, C. W. Machan, A. Y. S. Malkhasian, J. Agarwal and C. P. Kubiak, *Inorg. Chem.*, 2016, **55**, 3192–3198.

19 Z. Guo, G. Chen, C. Cometto, B. Ma, H. Zhao, T. Groizard, L. Chen, H. Fan, W.-L. Man, S.-M. Yiu, K.-C. Lau, T.-C. Lau and M. Robert, *Nat. Catal.*, 2019, **2**,

801–808.
20 A.-L. Robson, P. C. Dastoor, J. Flynn, W. Palmer, A. Martin, D. W. Smith, A. Woldu and S. Hua, *Front. Pharmacol.*, 2018, **9**, 80.
21 S. Bonnet, B. Limburg, J. D. Meeldijk, R. J. M. Klein Gebbink and J. A. Killian, *J. Am. Chem. Soc.*, 2011, **133**, 252–261.
22 R. S. Khnayzer, V. S. Thoi, M. Nippe, A. E. King, J. W. Jurss, K. A. El Roz, J. R. Long, C. J. Chang and F. N. Castellano, *Energy Environ. Sci.*, 2014, **7**, 1477–1488.
23 Y. Pellegrin and F. Odobel, *C. R. Chim.*, 2017, **20**, 283–295.
24 B. Limburg, E. Bouwman and S. Bonnet, *J. Phys. Chem. B*, 2016, **120**, 6969–6975.
25 G. B. Berselli, N. K. Sarangi, S. Ramadurai, P. V Murphy and T. E. Keyes, *ACS Appl. Bio Mater.*, 2019, **2**, 3404–3417.
26 S. Ramadurai, A. Kohut, N. K. Sarangi, O. Zholobko, V. A. Baulin, A. Voronov and T. E. Keyes, *J. Colloid Interface Sci.*, 2019, **542**, 483–494.
27 G. B. Berselli, A. V Gimenez, A. O'Connor and T. E. Keyes, *ACS Appl. Mater. Interfaces*, 2021, **13**, 29158–29169.
28 G. B. Berselli, N. K. Sarangi, A. V Gimenez, P. V Murphy and T. E. Keyes, *Chem. Commun.*, 2020, **56**, 11251–11254.
29 H. Basit, V. Gaul, S. Maher, R. J. Forster and T. E. Keyes, *Analyst*, 2015, **140**, 3012–3018.
30 L. M. Ickenstein, M. C. Sandström, L. D. Mayer and K. Edwards, *Biochim. Biophys. Acta - Biomembr.*, 2006, **1758**, 171–180.
31 K. Hashizaki, H. Taguchi, C. Itoh, H. Sakai, M. Abe, Y. Saito and N. Ogawa, *Chem. Pharm. Bull.*, 2003, **51**, 815–820.
32 T. Tabarin, A. Martin, R. J. Forster and T. E. Keyes, *Soft Matter*, 2012, **8**, 8743–8751.